Journal of Power Sources 196 (2011) 8815–8821

Contents lists available at ScienceDirect

Journal of Power Sources

journal homepage: www.elsevier.com/locate/jpowsour

# Effect of molybdenum content on structural, gaseous storage, and electrochemical properties of C14-predominant $AB_2$ metal hydride alloys

K. Young*, T. Ouchi, B. Huang, B. Reichman, M.A. Fetcenko

*Energy Conversion Devices Inc./Ovonic Battery Company, 2983 Waterview Drive, Rochester Hills, MI 48309, USA*

ARTICLE INFO

*Article history:*
Received 11 April 2011
Received in revised form 1 June 2011
Accepted 2 June 2011
Available online 13 June 2011

*Keywords:*
Hydrogen absorbing materials
Transition metal alloys
Metal hydride electrode
Electrochemical reactions

ABSTRACT

The structure, gaseous storage, and electrochemical properties of Mo-modified C14-predominant $AB_2$ metal hydride alloys were studied. The addition of Mo expands the unit cell volume and stabilizes the metal hydride. This increased metal-to-hydrogen bond strength reduces the equilibrium plateau pressure, reversible hydrogen storage, and the high-rate dischargeability in the flooded cell configuration, but not the high-rate dischargeability in the sealed cell configuration. The low-temperature performance was improved by the addition of Mo through increases in bulk diffusion rate, surface area, and surface catalytic ability. The increase in bulk diffusion is the result of smaller crystallites and larger $AB_2$–$AB_2$ grain boundary densities. The increase in surface area is due to the high solubility of Mo in alkaline solution. Even with a higher leaching rate, the Mo-containing alloys still have strong corrosion resistance which contributes positively to both the charge retention and the cycle life performances. As the Mo-content in the alloy increases, the low temperature performance improves at the expense of a lower capacity.



## 1. Introduction

Nickel metal hydride (Ni/MH) batteries have become the leading battery technology for hybrid electrical vehicles due to their superb abuse tolerance, calendar life, high rate charge acceptance, and environmental and safety performance. $AB_2$ alloys were proposed as the candidates to replace the current $AB_5$ alloys for higher capacity [1–3]. However, Ni/MH batteries using existing $AB_2$ and $AB_5$ metal hydride (MH) alloys are inferior to NiCd batteries in low-temperature high-power application [4,5]. Three elements, Cu [6–8], Fe [9–11], and Mo [12–16], have been identified to improve the low-temperature performance of $AB_5$ alloys and we have decided to start with Mo in a series of effort to improve the $AB_2$ MH alloys in the same application. In $AB_2$ alloy system, Mo shows the highest solubility compared to Mn, Zr, V, Cr, and Ti [17], increases the total hydrogen storage capacity (including the non-reversible part) [17,18], lowers the plateau pressure [19], facilitates the hydrogen diffusion in the bulk [20], shortens the activation process by increasing the surface porosity [18,21], increases the surface charge transfer resistance [18], improves both the low-temperature [13] and high-temperature [22] performance, but shortens cycle life [23–25]. Mo-substitution/addition in other hydrogen storage alloys, such as $AB_3$ [15,26–28], transitional metal based BCC alloys [29–32], and $AB_5$ [12,14,33–38], were reported previously. Since the results obtained so far are not all consistent, a more thoughtful study in this subject is necessary. In this report, we will focus on the effects of Mo-addition to the structures, gaseous phase storage, and electrochemical properties (especially at low temperature) of $AB_2$ MH alloys.

## 2. Experimental setup

In this study, induction melting was performed under an argon atmosphere in a 2 kg furnace using a $MgAl_2O_4$ crucible, an alumina tundish, and a steel pancake-shape mold. The chemical composition of each sample was examined by a Varian *Liberty* 100 inductively coupled plasma (ICP) system. A Philips *X'Pert Pro* x-ray diffractometer (XRD) was used to study the micro-structure, and a JOEL-*JSM6320F* scanning electron microscopy (SEM) with energy dispersive spectroscopy (EDS) capability was used to study the phase distribution and composition. Pressure-concentration-temperature (PCT) characteristics for each sample were measured using a Suzuki-Shokan multi-channel PCT system. In the PCT analysis, each sample was first activated by a two-hour thermal cycle between 300 °C and room temperature at 25 atm $H_2$ pressure. Then PCT isotherms at 30 °C and 60 °C were measured. Details of both electrode and cell preparations as well as measurement methods have been reported previously [39,40]. AC impedance measurements were conducted using Solartron 1250 Frequency Response Analyzer with sine wave of amplitude 10 mV and frequency range of 10 mHz to 10 kHz. Prior to the measurements, the electrodes were subjected to one full charge/discharge cycle at 0.1 C rate using

* Corresponding author. Tel.: +1 248 293 7000; fax: +1 248 299 4520.
*E-mail address:* kwoyoung@yahoo.com (K. Young).

0378-7753/$ – see front matter © 2011 Elsevier B.V. All rights reserved.
doi:10.1016/j.jpowsour.2011.06.010

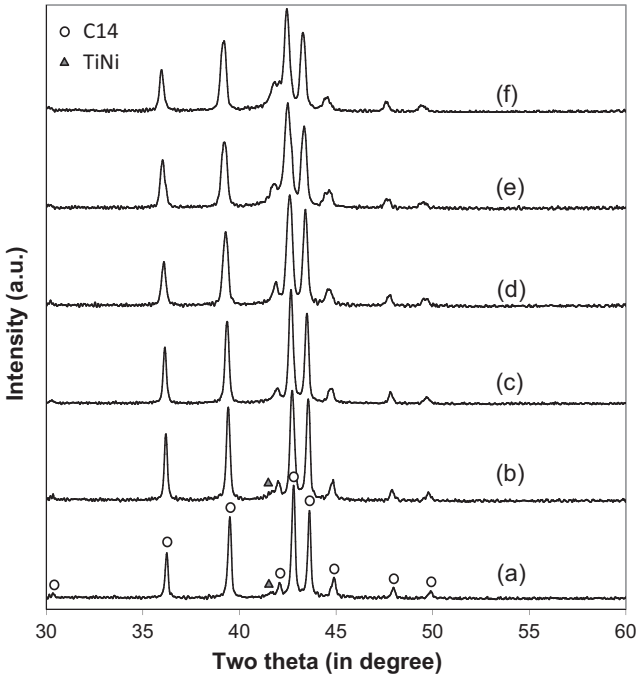


**Fig. 1.** XRD patterns using *Cu*-$K_\alpha$ as the radiation source for alloys Mo0 (a), Mo1 (b), Mo2 (c), Mo3 (d), Mo4 (e), and Mo5 (f).

Solartron 1470 Cell Test galvanostat, discharged to 80% state-of-charge (SOC), and then cooled to −40 °C.

## 3. Results and discussion

Six alloys with Mo substituting for Co at various levels from 0 to 5 at.% were prepared, and the design compositions are listed in Table 1. The base alloy (Mo0) with no Mo substitution was selected due to good high-rate dischargeability (HRD). The average electron density (*e*/*a*) for each alloy, calculated from the numbers of outer-shell electrons of the constituent elements, is listed in Table 1. Each *e*/*a* value is lower than the C14/C15 threshold of 7.0–7.1, and therefore a C14-predominant structure is anticipated [41,42]. The ICP results of all six alloys show very close values to the design compositions.

### 3.1. XRD structure analysis

The XRD patterns of the six alloys are shown in Fig. 1. Almost all peaks can be fit into a hexagonal C14 ($MgZn_2$) structure. The peak at around 41.5° corresponds to the B2 structured TiNi secondary phase [43]. This phase is the precursor of further solid-state transformation into $Zr_xNi_y$ type of secondary phases [44,45]. The lattice constants, *a* and *c*, calculated from the XRD patterns are listed in Table 1. As the amount of Mo increases, both *a* and *c* increase monotonically due to the larger atomic radius of Mo. This is proof that most Mo atoms reside in the B-site since Mo is smaller than Zr and Ti, but larger than the other B-site elements except for Al and Sn [46,47]. If most of the Mo atoms substitute Zr or Ti in the A-site, the lattice constants will reduce. The *a*/*c* aspect ratio decreases slightly with increasing Mo-content and predicts a higher degree of pulverization during cycling [48–50]. In the case of $ZrCr_{2-x}Mo_x$, the preference of Mo in the 2a sites over 6 h sites increases the *a*/*c* aspect ratio [51]. The 2a site forms two tetrahedrons with 6 h sites above and below. Therefore, the substitution with Mo in the 2a site will increase lattice constant *a* more than *c*. Our finding in the trend of *a*/*c* aspect ratio with the change in Mo-content is opposite and therefore a preference of Mo on the 6 h site in the current $ZrNi_2$-based alloy is proposed. The C14 unit cell volume also increases monotonically with the increase in Mo-content. The crystallite size was estimated by the Scherrer equation using the full-width at half the maximum (FWHM) of the C14 (1 0 3) peak in the XRD spectrum [52] and is listed in Table 1. As the amount of Mo increases, crystallite size becomes smaller, and consequently the $AB_2$–$AB_2$ grain boundary density increases and attributes to the bulk transportation of hydrogen, which will be discussed later in this paper.

### 3.2. SEM/EDS phase analysis

The microstructures for this series of alloys were studied by SEM and the back-scattering electron images (BEI) are presented in Fig. 2. Samples were mounted and polished on epoxy blocks, rinsed and dried before entering the SEM chamber. The compositions in several areas identified by numerical numbers in the micrographs were studied by EDS and the results are listed in Table 2. The Sn-content in each of the alloys is very small and was not detectable in most of the EDS measurements. Some B/A (stoichiometric number) and *e*/*a* values were also calculated and are listed in Table 2. Besides occasional $ZrO_2$ inclusions, the alloy is mainly composed of $AB_2$ as the major phase (with B/A around 2.0) and $Zr_xNi_y$ (can be TiNi, ZrNi, $Zr_7Ni_{10}$, $Zr_9Ni_{11}$ or combination) as the minor phase. The *e*/*a* values of the $AB_2$ phases are all below the C14/C15 threshold and correlate well with the C14-predominant structure. The amount of $Zr_xNi_y$ secondary phase is about the same for all six alloys in this study. This is an important observation since later on we cannot relate the higher bulk diffusion constant with the $AB_2$/$Zr_xNi_y$ grain boundary density. There is one high-vanadium phase (presumably BCC-structured) found in alloy Mo4.

### 3.3. Gaseous phase study

Gaseous phase hydrogen storage properties of the alloys were studied by PCT. The resulting absorption and desorption isotherms measured at 30 °C are shown in Fig. 3. The information obtained from the PCT study is summarized in Table 3. The plateau pressure increases by a small amount in the beginning and then decreases as the level of Mo increases in the alloy. Both positive and negative effects of Mo-substitution in the MH alloys on the hydrogen equilibrium pressure have been reported. On one hand, Mo is larger than most of the other B-site elements, and the expansion in lattice will increase the hydrogen storage site, make the hydride more stable, and lower the plateau pressure in most of the MH alloys [19,22,28,36]. On the other hand, Mo has the highest electronegativity in the group of B-site elements and will more strongly repel the extra electron brought in by hydrogen [34]. As low levels of Mo (1 at.%) are added, the lattice only expands by a small amount and does not have a large influence on the metal-to-hydrogen bond strength. According to Table 3, the plateau pressure increases slightly (difficult to see in Fig. 3a) because of the increase in electronegativity which is against further addition of hydrogen into the alloy. With more Mo added into the alloy, lattice expansion starts to play a more important role, and the plateau pressure decreases as a consequence.

The slope factor (SF) is defined as the ratio of the storage capacity between 0.01 and 0.5 MPa to the total capacity. SF of each alloy is listed in Table 3 and can be used to determine the degree of disorder in the alloy [46,53]. As the Mo-content increases, SF decreases monotonically and indicates that the degree of disorder increases. This result agrees with the smaller crystallite size found by XRD analysis. The hysteresis of the PCT isotherm, listed in Table 3, is defined as $\ln(P_a/P_d)$, where $P_a$ and $P_d$ are the absorption and desorption equilibrium pressures, respectively. The hysteresis can be used

**Table 1**
Design composition, $e/a$ average number of outer-shell electrons, lattice constants $a$ and $c$, $a/c$ ratio, C14 lattice volume, full width at half maximum ($2\theta$, in degrees) for (1 0 3) reflection peak, and corresponding crystallite size from XRD analysis.

| Alloy # | Ti at.% | Zr at.% | V at.% | Cr at.% | Mn at.% | Co at.% | Ni at.% | Al at.% | Sn at.% | Mo at.% | $e/a$ | $a$ (Å) | $c$ (Å) | $a/c$ | $V_{C14}$ (Å$^3$) | FWHM (1 0 3) | Crystallite Size (Å) |
|---|---|---|---|---|---|---|---|---|---|---|---|---|---|---|---|---|---|
| Mo0 | 12.0 | 21.5 | 10.0 | 7.5 | 8.1 | 8.0 | 32.2 | 0.4 | 0.3 | 0.0 | 6.82 | 4.9667 | 8.0974 | 0.6134 | 172.99 | 0.199 | 634 |
| Mo1 | 12.0 | 21.5 | 10.0 | 7.5 | 8.1 | 7.0 | 32.2 | 0.4 | 0.3 | 1.0 | 6.79 | 4.9709 | 8.1212 | 0.6121 | 173.79 | 0.215 | 558 |
| Mo2 | 12.0 | 21.5 | 10.0 | 7.5 | 8.1 | 6.0 | 32.2 | 0.4 | 0.3 | 2.0 | 6.76 | 4.9789 | 8.1299 | 0.6124 | 174.54 | 0.241 | 471 |
| Mo3 | 12.0 | 21.5 | 10.0 | 7.5 | 8.1 | 5.0 | 32.2 | 0.4 | 0.3 | 3.0 | 6.73 | 4.9877 | 8.1471 | 0.6122 | 175.52 | 0.315 | 326 |
| Mo4 | 12.0 | 21.5 | 10.0 | 7.5 | 8.1 | 4.0 | 32.2 | 0.4 | 0.3 | 4.0 | 6.70 | 4.9942 | 8.1712 | 0.6112 | 176.50 | 0.340 | 296 |
| Mo5 | 12.0 | 21.5 | 10.0 | 7.5 | 8.1 | 3.0 | 32.2 | 0.4 | 0.3 | 5.0 | 6.67 | 5.0004 | 8.1766 | 0.6116 | 177.06 | 0.323 | 315 |

to predict the pulverization rate of the alloy during cycling [48–50]. In this case, hysteresis increases with the increase in Mo-content, which agrees with the decreasing $a/c$ ratio by the correlation established previously [48–50]. Alloys with higher Mo-contents are more prone to pulverize during cycling.

With an increase in Mo-content, the maximum storage capacity decreases slightly, but the reversible storage capacity decreases monotonically as determined by PCT analysis (Table 3). The available hydrogen storage sites (about 3 per $AB_2$ formula) do not change with Mo-addition. However, the metal–hydrogen bond strength increases, which can be seen from the decrease in plateau pressure resulting from an increase in Mo-content. Therefore, the hydrogen becomes more difficult to be removed from the alloy.

Desorption equilibrium pressure at 0.75% storage capacities measured at 30 and 60 °C were used to calculate the changes in enthalpy ($\Delta H$) and entropy ($\Delta S$) by the equation

$$\Delta G = \Delta H - T\Delta S = RT \ln P \quad (1)$$

where $R$ is the ideal gas constant and $T$ is the absolute temperature. The results of these calculations are listed in Table 3. The absolute value of $\Delta H$ increases monotonically with increasing Mo-content and indicates that a more stable hydride has been formed. The $\Delta S$ values are very similar and close to the $\Delta S$ between the hydrogen gas and hydrogen in the solid [54].

### 3.4. Electrochemical measurement

Discharge capacities of the six alloys were measured in the flooded cell against the partially pre-charged $Ni(OH)_2$ as the positive electrode. Before the half-cell measurement, MH electrode was pre-activated in 30% KOH solution at 100 °C for 4 h. The initial discharge capacity before any charge input exists due to the hydrogen absorption generated as a result of the metal oxidation in the electrolyte. This capacity can be used to quantify the ease of activation [55]. A higher initial discharge capacity can be correlated to an easier oxidation/activation of the alloy. The amount of pre-

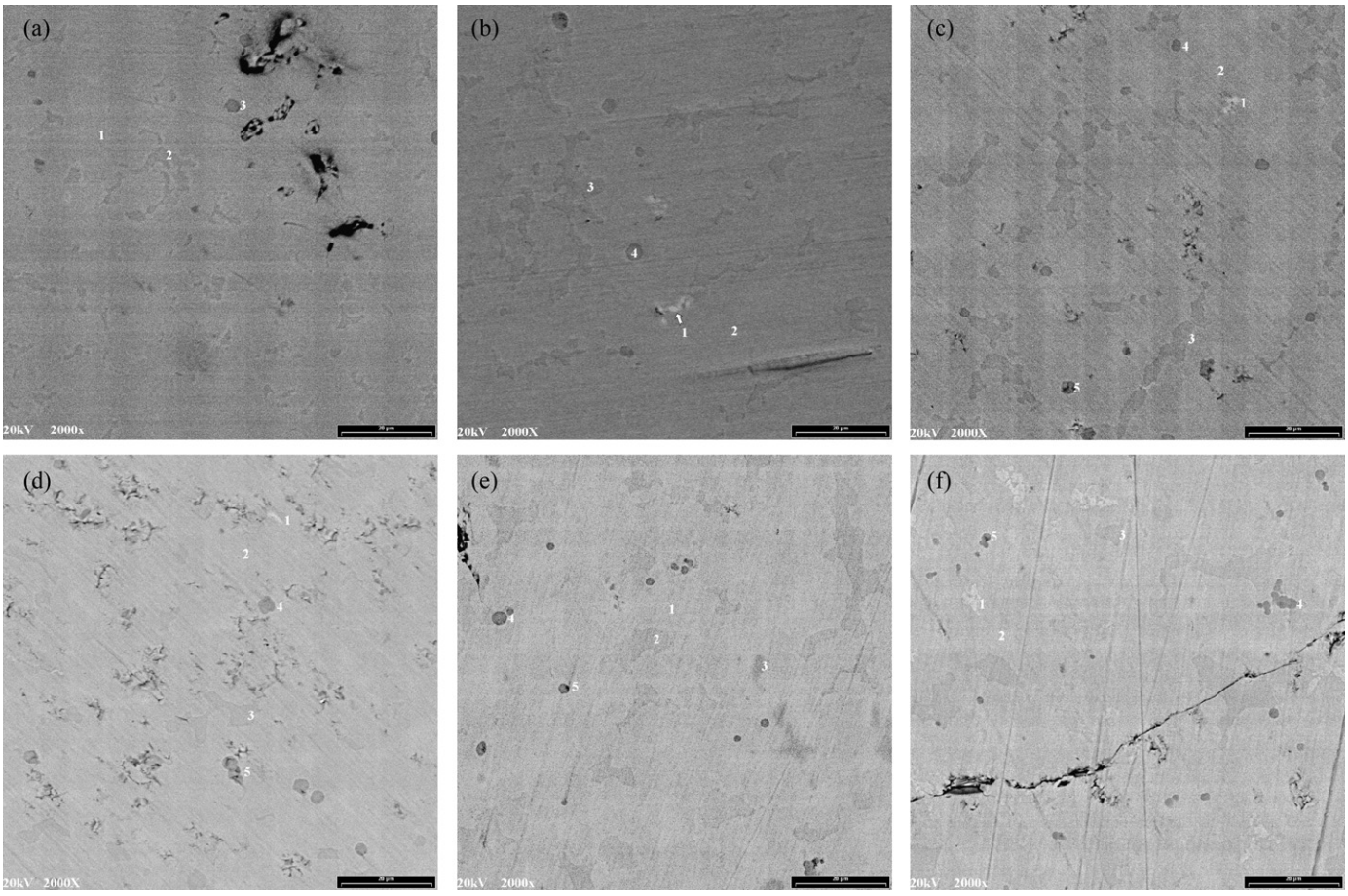


**Fig. 2.** SEM backscattering images for alloys Mo0 (a), Mo1 (b), Mo2 (c), Mo3 (d), Mo4 (e), and Mo5 (f).

**Table 2**
EDS result in atomic percentages from area identified in SEM micrograph (Fig. 2).

| Alloy # | Ti | Zr | V | Ni | Co | Mn | Cr | Al | Mo | Sn | B/A | *e*/*a* | Phase |
|---|---|---|---|---|---|---|---|---|---|---|---|---|---|
| Mo0-1 | 14.6 | 19.4 | 8.6 | 38.3 | 6.4 | 7.5 | 5.1 | 0.0 | 0.0 | 0.1 | 1.9 | 7.03 | $AB_2$ |
| Mo0-2 | 23.3 | 18.0 | 3.0 | 45.6 | 5.1 | 3.5 | 1.4 | 0.0 | 0.0 | 0.1 | 1.4 | | $Zr_xNi_y$ |
| Mo0-3 | 3.9 | 80.4 | 3.4 | 6.2 | 1.3 | 2.1 | 2.2 | 0.0 | 0.0 | 0.5 | | | $ZrO_2$ |
| Mo1-1 | 7.4 | 67.3 | 4.3 | 12.5 | 2.3 | 3.1 | 2.8 | 0.4 | 0.0 | 0.0 | | | Zr–metal |
| Mo1-2 | 11.0 | 22.3 | 11.7 | 27.0 | 7.5 | 9.4 | 9.2 | 0.9 | 1.2 | 0.0 | 2.0 | 6.60 | $AB_2$ |
| Mo1-3 | 26.5 | 17.9 | 1.1 | 47.1 | 4.2 | 2.1 | 0.3 | 0.9 | 0.1 | 0.0 | 1.3 | | $Zr_xNi_y$ |
| Mo1-4 | 0.8 | 95.6 | 0.5 | 1.9 | 0.3 | 0.2 | 0.2 | 0.4 | 0.0 | 0.0 | | | $ZrO_2$ |
| Mo2-1 | 10.3 | 59.6 | 4.5 | 15.5 | 2.7 | 3.8 | 2.6 | 0.0 | 1.1 | 0.0 | | | Zr–metal |
| Mo2-2 | 10.5 | 20.1 | 12.0 | 29.1 | 6.6 | 9.5 | 9.4 | 0.3 | 2.6 | 0.0 | 2.3 | 6.72 | $AB_2$ |
| Mo2-3 | 25.6 | 15.5 | 1.8 | 49.5 | 4.1 | 2.6 | 0.6 | 0.1 | 0.2 | 0.0 | 1.4 | | $Zr_xNi_y$ |
| Mo2-4 | 5.6 | 78.2 | 2.4 | 8.9 | 0.8 | 1.5 | 1.2 | 0.0 | 1.4 | 0.0 | | | $ZrO_2$ |
| Mo2-5 | 9.2 | 20.3 | 12.0 | 26.3 | 6.6 | 10.5 | 11.6 | 0.4 | 3.1 | 0.0 | 2.3 | 6.63 | $AB_2$ |
| Mo3-1 | 16.0 | 20.9 | 6.4 | 41.0 | 4.0 | 6.2 | 3.9 | 0.2 | 1.5 | 0.0 | 1.7 | 7.02 | $TiNi + AB_2$ |
| Mo3-2 | 10.1 | 20.0 | 12.0 | 28.7 | 5.6 | 9.8 | 9.6 | 0.2 | 4.0 | 0.0 | 2.2 | 6.69 | $AB_2$ |
| Mo3-3 | 25.9 | 16.8 | 1.3 | 48.9 | 3.6 | 2.4 | 0.5 | 0.2 | 0.4 | 0.0 | 1.3 | | $Zr_xNi_y$ |
| Mo3-4 | 7.3 | 53.6 | 7.0 | 16.3 | 2.5 | 5.1 | 5.0 | 0.2 | 3.1 | 0.0 | | | $ZrO_2$ |
| Mo3-5 | 8.4 | 59.6 | 3.7 | 19.5 | 1.8 | 3.1 | 2.4 | 0.0 | 1.5 | 0.0 | | | $ZrO_2$ |
| Mo4-1 | 10.7 | 20.3 | 10.8 | 30.8 | 4.8 | 10.2 | 8.5 | 0.2 | 3.7 | 0.0 | 2.2 | 6.74 | $AB_2$ |
| Mo4-2 | 25.8 | 17.5 | 1.0 | 48.8 | 3.6 | 2.5 | 0.4 | 0.0 | 0.4 | 0.0 | 1.3 | | $Zr_xNi_y$ |
| Mo4-3 | 5.1 | 2.1 | 35.5 | 3.8 | 0.9 | 5.9 | 22.2 | 0.0 | 24.5 | 0.0 | 12.9 | | BCC |
| Mo4-4 | 19.7 | 28.5 | 1.3 | 43.0 | 3.1 | 2.4 | 0.7 | 0.9 | 0.3 | 0.0 | 1.1 | | $Zr_xNi_y$ |
| Mo4-5 | 7.6 | 55.6 | 4.9 | 20.2 | 2.0 | 4.7 | 3.1 | 0.4 | 1.6 | 0.0 | | | $ZrO_2$ |
| Mo5-1 | 10.9 | 19.9 | 11.0 | 31.3 | 3.4 | 9.8 | 8.5 | 0.0 | 5.2 | 0.0 | 2.2 | 6.73 | $AB_2$ |
| Mo5-2 | 11.5 | 20.3 | 10.1 | 32.9 | 3.5 | 9.6 | 7.9 | 0.2 | 4.0 | 0.0 | 2.1 | 6.77 | $AB_2$ |
| Mo5-3 | 24.5 | 18.9 | 1.4 | 48.9 | 2.6 | 2.4 | 0.5 | 0.1 | 0.7 | 0.0 | 1.3 | | $Zr_xNi_y$ |
| Mo5-4 | 6.6 | 77.3 | 0.7 | 12.8 | 0.4 | 1.0 | 0.4 | 0.0 | 0.8 | 0.0 | | | $ZrO_2$ |
| Mo5-5 | 10.5 | 38.5 | 4.6 | 33.2 | 1.9 | 5.5 | 2.8 | 1.2 | 1.8 | 0.0 | 1.0 | | $Zr_xNi_y$ |

charge in mAh $g^{-1}$ for each alloy is listed in Table 3. The alloy surface becomes very corrosion-resistant with any level of Mo-addition, which was reported by Li et al. [18]. However, the highest solubility of Mo among the elements in the alloy also increases the surface area by a large amount [17]. It is not common to have an additive which increases the surface area and still maintains the corrosion-resistant nature.

Discharge capacities of the first cycle at different discharge rates after activation are plotted in Fig. 4. The discharge capacities at 300 and 5 mA $g^{-1}$ are listed in Table 3. The discharge capacity increases at low substitution levels of Mo and then decreases at high substitution levels. The trend is similar to the evolution of PCT plateau pressure but not to that of the gaseous phase storage capacity. The difference between hydrogen storages in the gaseous phase and electrochemically resides in the surface. While a clean, fresh, and recently exposed surface in gaseous phase is important, the structure and composition of the surface oxide and the embedded metallic inclusions are important for the electrochemical storage and discharge of hydrogen [56]. The addition of Mo changes the surface properties (porosity, metallic cluster composition, oxide thickness, etc.) and thus changes the evolution of electrochemical capacity.

Half-cell HRD of each alloy, defined as the ratio of discharge capacity measured at 300 mA $g^{-1}$ to that measured at 5 mA $g^{-1}$, is listed in Table 3. In a flooded cell, the half-cell HRD value decreases with the increase in Mo-content. The result is consistent with the decrease in plateau pressure, the decrease in reversible gaseous phase hydrogen storage, and the increase in $|\Delta H|$, which are all

**Table 3**
Summary of gas phase properties (plateau pressure, slope factor, hysteresis, and maximum capacity), and results from half-cell measurement (pre-charge, capacity, high-rate dischargeability, diffusion coefficient, and exchange current density) and full-cell (cycle life, charge retention, specific power, and low-temperature performance) measurement.

| | Des. pressure at 0.75%, at 30 °C (Torr) | Slope factor at 30 °C (%) | PCT hysteresis at 0.75%, at 30 °C | Max. cap. at 30 °C (wt.%) | Reversible cap. at 30 °C (wt.%) | $-\Delta H$ (kJ $mol^{-1}$) | $-\Delta S$ (J $mol^{-1}$) | Pre-charge (mAh $g^{-1}$) | Cap at 300 mA $g^{-1}$ (mAh $g^{-1}$) | Cap at 5 mA $g^{-1}$ (mAh $g^{-1}$) |
|---|---|---|---|---|---|---|---|---|---|---|
| Mo0 | 387 | 80.8 | 0.05 | 1.49 | 1.38 | 33.7 | 105 | 15 | 311 | 366 |
| Mo1 | 404 | 80.0 | 0.07 | 1.46 | 1.33 | 35.4 | 111 | 2 | 317 | 376 |
| Mo2 | 370 | 78.1 | 0.07 | 1.43 | 1.24 | 36.4 | 114 | 7 | 320 | 384 |
| Mo3 | 247 | 67.3 | 0.14 | 1.46 | 1.21 | 36.7 | 111 | 3 | 280 | 370 |
| Mo4 | 139 | 64.9 | 0.29 | 1.44 | 1.16 | 37.8 | 111 | 3 | 284 | 375 |
| Mo5 | 130 | 64.6 | 0.41 | 1.42 | 1.08 | 38.7 | 112 | 1 | 273 | 364 |

| | HRD | Diffusion coefficient ($10^{-10}$ $cm^2$ $s^{-1}$) | Exchange current (mA $g^{-1}$) | 70% cycle life | 30 days charge retention (%) | Room temp. specific power (W $kg^{-1}$) | Low-temp. −10 °C, 0.5 C (%) | Charge transfer resistance at −40 °C (Ω g) | Double-layer capacitance at −40 °C (Farad $g^{-1}$) |
|---|---|---|---|---|---|---|---|---|---|
| Mo0 | 0.850 | 2.5 | 22.5 | 225 | 18 | 151 | 44 | 70.4 | 0.120 |
| Mo1 | 0.843 | 5.8 | 27.9 | 350 | 19 | 157 | 65 | 59.0 | 0.155 |
| Mo2 | 0.833 | 4.1 | 20.8 | 355 | 16 | 162 | 63 | 40.2 | 0.184 |
| Mo3 | 0.757 | 5.1 | 24.3 | 355 | 22 | 168 | 74 | 53.1 | 0.152 |
| Mo4 | 0.757 | 7.3 | 35.3 | 350 | 32 | 165 | 94 | 28.3 | 0.297 |
| Mo5 | 0.750 | 5.6 | 34.1 | 360 | 38 | 169 | 96 | 29.3 | 0.228 |

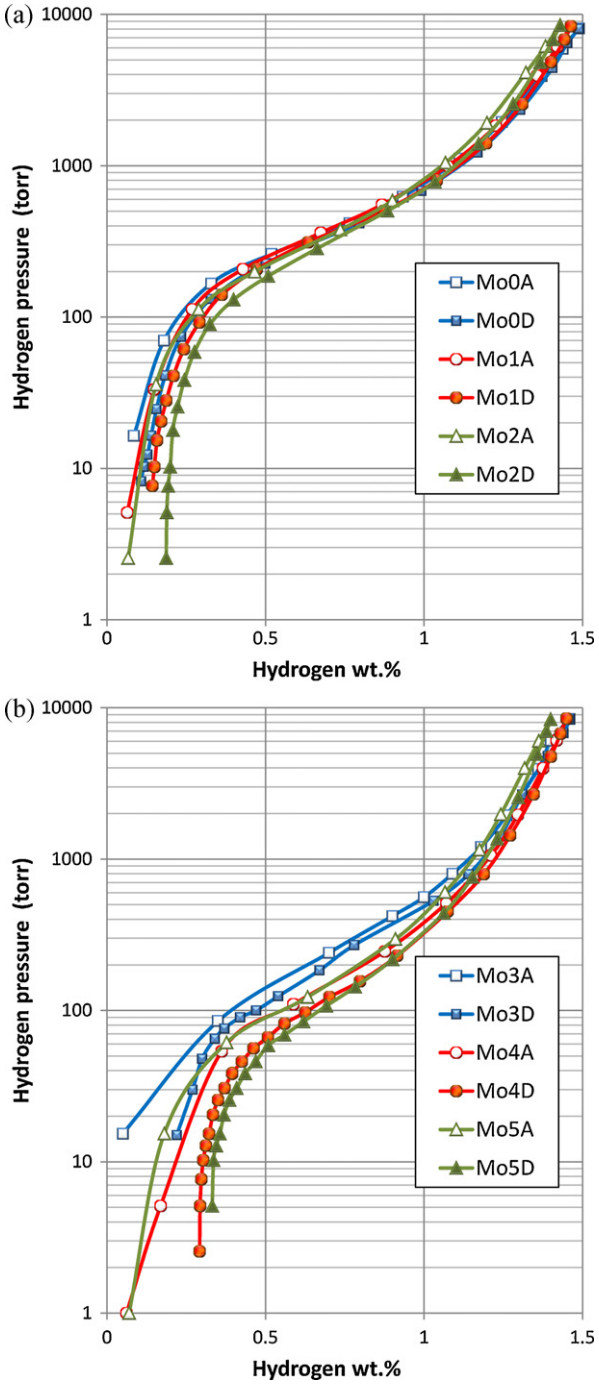


**Fig. 3.** 30 °C PCT isotherms of alloys Mo0, Mo1, and Mo2 (a) and Mo3, Mo4, and Mo5 (b). Open and solid symbols are for absorption and desorption curves, respectively.

related to the metal–hydrogen bond strength. The surface reaction is not a determining factor for the half-cell HRD as in the case of flooded cell testing.

Besides the metal–hydrogen bond strength, both the bulk diffusion coefficient ($D$) and the surface exchange current ($I_o$) are important parameters for analyzing the MH alloy for use in a sealed Ni/MH battery. The details in measuring both parameters were reported previously [57], and the values are listed in Table 3. In most cases, the Mo-containing alloys have higher $D$ and $I_o$ values than those of Mo-free alloy. The improvement in bulk diffusion by adding Mo is due to the increase in the $AB_2$–$AB_2$ grain boundary density as seen from the XRD analysis, which was also reported in many different alloy systems [26,27,37]. Since XRD analysis shows similar $Zr_xNi_y$ abundance (known to be important in the electrochemical properties of the alloys [58,59]), the increase in bulk diffusion is not due to the change in the $AB_2$–$Zr_xNi_y$ interface density. The increase in exchange current is due to the highly porous surface created by leaching out Mo into the electrolyte [20,21], which has also been reported in different alloy systems [13–15,26,34,35,37].

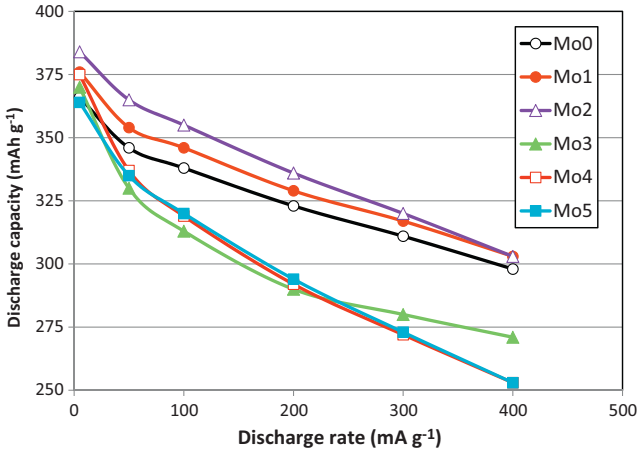


**Fig. 4.** The rate-dependency of discharge capacity from half-cell measurement for alloys Mo0 to Mo5.

Four important Ni/MH technical parameters (cycle life, charge retention, specific power, and low-temperature performance) for the MH electrode made from each alloy are listed in Table 3. Alloys with Mo addition show similar cycle life performances (measured by the number of cycles to reach 70% of the original capacity) which are all better than that of the Mo-free Mo0 alloy. Therefore, the addition of Mo, regardless of the substitution level, is beneficial to the cycle life performance. The surface of Mo-containing alloys, although highly porous, has strong resistance against oxidation as seen from the low pre-charge capacity observed in the half-cell measurement. Although the large PCT hysteresis in the alloy with higher Mo-substitution predicts a high pulverization rate during cycling, the anti-corrosive nature in the Mo-containing surface prevents further decay in capacity during cycling. This finding is different from previous reports on Mo-modified C14-based Cr-free $AB_2$ alloys [23–25]. Without the formation of Cr–V solid solution, the $AB_2$ alloys suffer from low cycle life due to the high solubility of vanadium in alkaline solution [60]. The Mo-addition to these Cr-free alloys increases the decomposition at the alloy surface and contributes to a shorter life.

Charge retention test results are plotted in Fig. 5, and the 30-day charge retention values are listed in Table 3. Charge retention increases monotonically with the increase in Mo due to the more corrosion-resistant nature of the surface. The room temperature specific power densities measured at 80% SOC are listed in Table 3. Despite the decreasing HRD values from the half-cell experiment, the specific power increases monotonically with the increase in Mo-content. The result is in agreement with the bulk diffusion and surface exchange current studies. In a sealed Ni/MH cell, the surface is semi-starved with electrolyte. Electrolyte is limited to allow rapid gas recombination during overcharge and overdischarge. Without a total flooding on the surface, the surface reaction and bulk transport property become more important in determining the high-rate performance.

The low-temperature characteristic is believed to correlate strongly with high-power performance [40], and the result from the current study is in complete agreement with previous reports. Low-temperature performance, defined as the ratio of the capacity measured at 0.5 C rate and −10 °C to the capacity measured

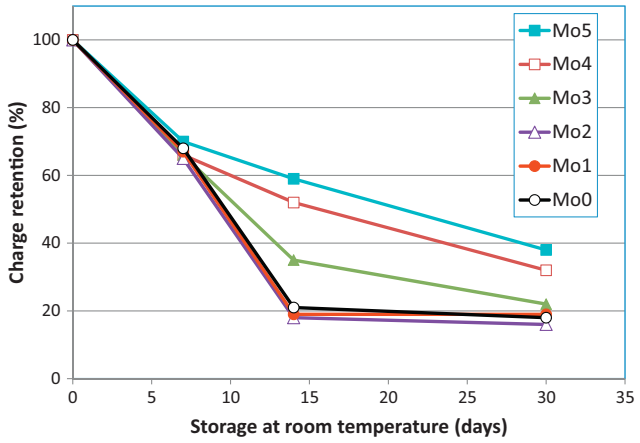


**Fig. 5.** The charge retention measured at room temperature for alloys Mo0 to Mo5 in the sealed cell configuration.

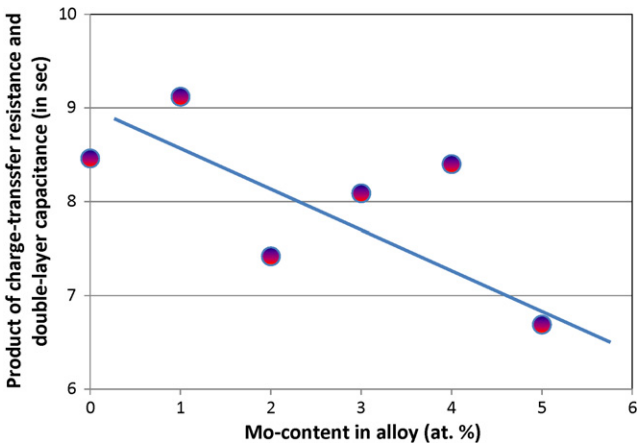


**Fig. 7.** The product of charge-transfer resistance and double-layer capacitance measured at −40 °C as a function of Mo-content.

at the same rate and room temperature, is listed in Table 3 and plotted in Fig. 6. Alloys with more Mo have better low temperature performance, which follows the same trend of the high-rate characteristic. Therefore, Mo is proven to be beneficial to low-temperature application due to the larger grain boundary in the bulk and larger surface area. A more detailed investigation of the surface oxide, including micro-porosity and embedded metallic inclusions, is planned in the future.

The low-temperature characteristics of these alloys were further studied by the AC impedance measurement conducted at −40 °C. The charge-transfer resistance and double-layer capacitance were calculated from the Cole–Cole plot and are listed in Table 3. In general, at −40 °C, the charge-transfer resistance decreases and the capacitance increase as the Mo-content increases. Since the capacitance is proportional to the surface area, this measurement is direct proof of the increasing surface area due to the ease leaching of Mo into the electrolyte is obtained. In order to further understand the improvement in low-temperature performance, the product of charge-transfer resistance and double-layer capacitance was plotted against the Mo-content in Fig. 7. This product removes the contribution from surface area and generally decreases as Mo-content increases. This implies that the presence of Mo in the surface also improves the inherit catalytic property of the alloy. In the past, Jakšić also reported a dramatic reduction in surface hydrogen evolution over-potential in the alloy co-deposited galvanically with Mo and Co [61]. Thus the improvement in low-temperature performance by Mo-addition is due to a combination of an increase in the surface area and an increase in the surface catalytic ability.

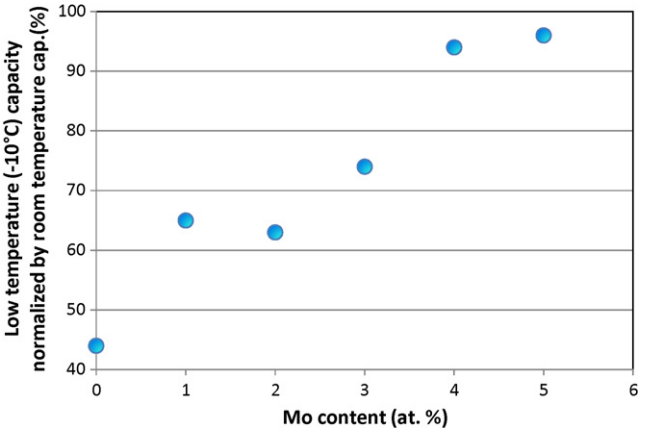


**Fig. 6.** Low temperature performance of Mo-substituted alloys determined by the capacity measured at 0.5 C rate and −10 °C normalized to the capacity measured at the same rate and room temperature vs. Mo-content.

## 4. Summary

Mo was studied as a modifier to C14-predominant $AB_2$ alloys. The addition of Mo increases both lattice constants and the aspect $a/c$ ratio due to the preference in substitution site. The expansion in unit cell volume makes the hydride more stable and consequently lowers the equilibrium plateau pressure, lowers the gaseous phase reversible storage capacity, increases the absolute value of $\Delta H$, and lowers the HRD in the half-cell configuration. Incorporation of Mo also increases the diffusion coefficient, the surface area, the surface exchange current, specific power, and most importantly, improves the low-temperature performance, but at the expense of a lower capacity. The corrosion resistance of the surface also increases and contributes positively to both the charge retention and cycle life performance.

## References

[1] S.R. Ovshinsky, M.A. Fetcenko, J. Ross, Science 260 (1993) 176.
[2] M.A. Fetcenko, S.R. Ovshinsky, K. Young, B. Reichman, C. Fierro, J. Koch, F. Martin, W. Mays, T. Ouchi, B. Sommers, A. Zallen, J. Alloys Compd. 330/332 (2002) 752.
[3] M.A. Fetcenko, S.R. Ovshinsky, B. Reichman, K. Young, C. Fierro, J. Koch, A. Zallen, W. Mays, T. Ouchi, J. Power Sources 165 (2007) 544.
[4] D. Linden, in: D. Linden (Ed.), Handbook of Batteries, 2nd ed., McGraw-Hill, Inc., New York, 1995, p. 28.19 and 33.10.
[5] M. Oshitani, in: H. Tamura (Ed.), Hydrogen Storage Alloys–Fundamentals and Frontier Technologies, NTS Inc., Tokyo, 1998, p. 569.
[6] S. Kim, H. Lee, K. Cho, J. Lee, J. Alloys Compds. 282 (1999) 261.
[7] K. Young, T. Ouchi, M.A. Fetcenko, U.S. Patent 7,344,677, 2008.
[8] K. Young, T. Ouchi, A. Banik, J. Koch, M.A. Fetcenko, L.A. Bendersky, K. Wang, J. Alloys Compd. 509 (2011) 4896.
[9] M.A. Fetcenko, US Patent 5,096,667, 1992.
[10] M.A. Fetcenko, S.R. Ovshinsky, US Patent 5,104,617, 1992.
[11] H. Yang, Y. Chen, M. Tao, C. Wu, J. Shao, G. Deng, Electrochim. Acta 55 (2010) 648.
[12] P.H.L. Notten, P. Hokkeling, J. Electrochem. Soc. 138 (1991) 1877.
[13] Y. Tsuji, O. Yamamoto, Y. Yamamura, H. Seri, Y. Toyoguchi, US Patent 5,753,054, 1998.
[14] H. Senoh, Y. Hara, H. Inoue, C. Iwakura, Electrochim. Acta 46 (2001) 967.
[15] X.B. Zhang, D.Z. Sun, W.Y. Yin, Y.J. Chai, M.S. Zhao, Electrochim. Acta 50 (2005) 3407.
[16] K. Young, T. Ouchi, B. Reichman, J. Koch, M.A. Fetcenko, J. Alloys Compd. 509 (2011) 3995.
[17] M. Au, F. Pourarian, S.G. Sankar, W.E. Wallace, L. Zhang, Mater. Sci. Eng. B 33 (1995) 53.
[18] S. Li, M. Zhao, L. Wang, Y. Liu, Y. Wang, Mater. Sci. Eng. B 150 (2008) 168.
[19] T. Huang, Z. Wu, B. Xia, N. Xu, Mater. Sci. Eng. A 397 (2005) 284.
[20] J. Chen, S.X. Dou, H.K. Liu, J. Alloys Compd. 256 (1997) 40.
[21] M. Wen, Y. Zhai, Eng. Chem. Metall. 21 (2000) 331.
[22] C. Jeong, W. Chung, C. Iwakura, I. Kim, J. Power Sources 79 (1999) 19.

[23] M.Y. Song, I.H. Kown, D.S. Ahn, M.S. Sohn, Metals Mater. Int. 7 (2001) 257.
[24] M.Y. Song, D. Ahn, I.H. Kwon, S.H. Chough, J. Electrochem. Soc. 148 (2001) A1041.
[25] S. Han, M. Zhao, L. Wu, Y. Zheng, Chem. J. Chin. Univ. 24 (2003) 2256.
[26] X.B. Zhang, D.Z. Sun, W.Y. Yin, Y.J. Chai, M.S. Zhao, Eur. J. Inorg. Chem. (2005) 2235.
[27] X. Zhang, S. Sun, W. Yin, Y. Chai, M. Zhao, J. Power Sources 154 (2006) 290.
[28] S. Shi, C. Li, W. Tang, J. Alloys Compd. 476 (2009) 874.
[29] A. Kamegawa, T. Tamura, H. Takamura, M. Okada, J. Alloys Compd. 356/357 (2003) 447.
[30] K. Kubo, H. Itoh, T. Takahashi, T. Ebisawa, T. Kabutomori, Y. Nakamura, E. Akiba, J. Alloys Compd. 356/357 (2003) 452.
[31] K. Iwase, Y. Nakamura, K. Mori, S. Harjo, T. Ishigaki, T. Kamiyama, E. Akiba, J. Alloys Compd. 404/406 (2005) 99.
[32] M. Okada, T. Chou, A. Kamegawa, T. Tamura, H. Takamura, A. Matsukawa, S. Yamashita, J. Alloys Compd. 356/357 (2003) 480.
[33] M.T. Yeh, V.M. Beibutian, S.E. Hsu, J. Alloys Compd. 293/295 (1999) 721.
[34] H. Ye, H. Zhang, Adv. Eng. Mater. 3 (2001) 481.
[35] C. Iwakura, H. Senoh, K. Morimoto, Y. Hara, H. Inoue, Electrochemistry 70 (2002) 2.
[36] S.E. Hsu, V.M. Beibutian, M.T. Yeh, J. Alloys Compd. 330/332 (2002) 882.
[37] H. Ye, H. Zhang, J. Grad. Sch. Chin. Acad. Sci. 20 (2003) 381.
[38] S. Srivastava, R.K. Upadhyay, J. Power Sources 195 (2010) 2996.
[39] K. Young, M.A. Fetcenko, T. Ouchi, F. Li, J. Koch, J. Alloys Compd. 464 (2008) 238.
[40] K. Young, M.A. Fetcenko, J. Koch, K. Morii, T. Shimizu, J. Alloys Compd. 486 (2009) 559.
[41] Z. Shi, S. Chumbley, F.C. Laabs, J. Alloys Compd. 312 (2000) 41.
[42] J.H. Zhu, P.K. Liaw, C.T. Liu, Mater. Sci. Eng. A239/240 (1997) 260.
[43] K. Young, J. Nei, T. Ouchi, M.A. Fetcenko, J. Alloys Compd. 509 (2011) 2277.
[44] W.J. Boettinger, D.E. Newbury, K. Wang, L.A. Bendersky, C. Chiu, U.R. Kattner, K. Young, B. Chao, Metall. Mater. Trans. A 41 (2010) 2033.
[45] L.A. Bendersky, K. Wang, W.J. Boettinger, D.E. Newbury, K. Young, B. Chao, Metall. Mater. Trans. A 41 (2010) 1891.
[46] K. Young, T. Ouchi, J. Koch, M.A. Fetcenko, J. Alloys Compd. 477 (2009) 749.
[47] K. Young, M.A. Fetcenko, T. Ouchi, F. Li, J. Koch, J. Alloys Compd. 469 (2009) 406.
[48] K. Young, T. Ouchi, M.A. Fetcenko, J. Alloys Compd. 480 (2009) 428.
[49] K. Young, T. Ouchi, W. Mays, B. Reichman, M.A. Fetcenko, J. Alloys Compd. 480 (2009) 434.
[50] K. Young, T. Ouchi, M.A. Fetcenko, J. Alloys Compd. 480 (2009) 440.
[51] M. Bououdina, J.L. Soubeyroux, P. de Rango, D. Fruchart, Int. J. Hydrogen Energy 25 (2000) 1059.
[52] H.P. Klug, L.E. Alexander, X-ray Diffraction Procedures for Polycrystalline and Amorphous Materials, 2nd ed., John Wiley & Sons, New York, 1974, p. 656.
[53] K. Young, T. Ouchi, M.A. Fetcenko, R.K. Regmi, G. Lawes, J. Alloys Compd. 490 (2010) 282.
[54] L. Schlapbach, A. Züttle, Nature 414 (2001) 353.
[55] C. Iwakura, W.K. Choi, S. Zhang, H. Inoue, Electrochim. Acta 44 (1998) 1677.
[56] K. Young, B. Huang, R.K. Regmi, G. Lawes, Y. Liu, J. Alloys Compd. 506 (2010) 831.
[57] F. Li, K. Young, T. Ouchi, M.A. Fetcenko, J. Alloys Compd. 471 (2009) 371.
[58] A. Visintin, H.A. Peretti, F. Ruiz, H.L. Corso, W.E. Triaca, J. Alloys Compd. 428 (2007) 244.
[59] K. Young, T. Ouchi, G. Huang, B. Chao, M.A. Fetcenko, L.A. Bendersky, K. Wang, C. Chiu, J. Alloys Compd. 509 (2011) 4896.
[60] K. Young, M.A. Fetcenko, S.R. Ovshinsky, T. Ouchi, B. Reichman, W. Mays, in: G. Jerkiewicz, J.M. Feliu, B.N. Popov (Eds.), Hydrogen at Surface and Interface, Electrochemical Society Proceedings, vol. 6, 2000, p. 60.
[61] M.M. Jakšić, Int. J. Hydrogen Energy 11 (1986) 519.